The Impact of Phase Retention on the Structural and Optoelectronic Properties of Metal Halide Perovskites

Osherov, Anna; Hutter, Eline M.; Galkowski, Krzysztof; Brenes, Roberto; Maude, Duncan K.; Nicholas, Robin J.; Plochocka, Paulina; Bulović, Vladimir; Savenije, Tom J.; Stranks, Samuel D.

DOI
10.1002/adma.201604019

Publication date
2016

Document Version
Final published version

Published in
Advanced Materials

Citation (APA)
Osherov, A., Hutter, E. M., Galkowski, K., Brenes, R., Maude, D. K., Nicholas, R. J., Plochocka, P., Bulović, V., Savenije, T. J., & Stranks, S. D. (2016). The Impact of Phase Retention on the Structural and Optoelectronic Properties of Metal Halide Perovskites. *Advanced Materials*, *28*(48), 10757-10763. https://doi.org/10.1002/adma.201604019

The Impact of Phase Retention on the Structural and Optoelectronic Properties of Metal Halide Perovskites

*Anna Osherov, Eline M. Hutter, Krzysztof Galkowski, Roberto Brenes, Duncan K. Maude, Robin J. Nicholas, Paulina Plochocka, Vladimir Bulović, Tom J. Savenije, and Samuel D. Stranks**

Metal halide perovskites such as methylammonium lead iodide ($MAPbI_3$, MA = CH_3NH_3) are highly promising materials for a variety of low-cost optoelectronic applications including solar cells, light-emitting diodes, lasers, and photodetectors.[1,2] The perovskite in these devices is typically deposited as a thin film from simple precursor salts and the resulting polycrystalline films show crystalline character.[3] This in part contributes to their superlative properties that render them fitting for the aforementioned devices, most notably long charge carrier diffusion lengths,[4] strong absorption coefficients,[5] and low levels of nonradiative decay,[2,6] the latter which could enable perovskite devices to approach their radiative efficiency limits.[7]

The metal halide perovskite class of ionic materials is mechanically "softer" compared to other efficient photovoltaic materials.[8] This results in a variety of curious phenomena including large ionic displacements through photo-[9] and field-induced[10] ion migration and light-induced structural[11] rearrangements. Another consequence of the soft nature is the relatively easy reorientation of its crystal structure to undergo phase transitions. $MAPbI_3$ exists in the tetragonal phase (TP) at room temperature (≈150 K < T < 330 K) but undergoes a rearrangement to an orthorhombic phase (OP) at low temperature (T ≈ 150 K) and a cubic phase at high temperature (T ≈ 330 K).[12] Recent device[13] and spectroscopic[14] studies suggest that there is no marked operational distinction between the tetragonal and cubic phases for polycrystalline films, with the photoluminescence (PL) monotonically blue-shifting upon raising the temperature following the same spectral evolution with temperature as seen within the tetragonal phase. In contrast, the low-temperature tetragonal–orthorhombic phase (TP–OP) transition leads to a substantial perturbation in the optoelectronic properties of polycrystalline films, with clear changes observed in device behavior,[13,15] recombination kinetics,[16,17] and bandgap.[18] The specific onset of the TP–OP transition temperature has been reported to be in the range 140–170 K[18–20] and appears to depend strongly on the perovskite processing route[19] and grain size.[21] Furthermore, there have been reports of hysteretic behavior in the optical[18,22] and transport[21] properties of these materials in cooling/heating cycles through the low-temperature phase transition, suggesting that the phase transition also depends on the history of the temperature of the sample.

We and others have reported that there is a grain-to-grain heterogeneity on the microscale in optoelectronic properties of the polycrystalline perovskite films, which limits device performance.[23,24] This microscale heterogeneity has been observed in emission,[23–25] absorption,[26] and device photocurrent[27,28] even for high-performing device materials, suggesting that there is substantial room for further improvement of these properties. Kong et al.[29] and Panzer et al.[30] reported that there is a coexistence of both OP and TP components below the low-temperature phase transition and it has been proposed that this results from small inclusions adopting the room-temperature phase at low temperature.[18] However, a direct connection between these bulk and microscale photophysical observations, the structure of the perovskites, and the hysteretic phase observations is lacking. This information is essential for understanding the photophysics of these curious semiconductors and to ultimately achieving the homogeneity in structural and optoelectronic properties required to reach device efficiency limits.

Here, we use temperature-dependent X-ray diffraction (XRD) measurements to study the structural changes around the low-temperature (TP–OP) phase transition of polycrystalline $MAPbI_3$ perovskite thin films prepared using a lead acetate precursor recipe on silicon substrates. We find direct evidence for the coexistence of the OP and TP above and below the phase transition temperature and a stark difference between the two

Dr. A. Osherov, R. Brenes, Prof. V. Bulović, Dr. S. D. Stranks
Research Laboratory of Electronics
Massachusetts Institute of Technology
77 Massachusetts Avenue, Cambridge, MA 02139, USA
E-mail: sds65@cam.ac.uk
E. M. Hutter, Dr. T. J. Savenije
Opto-electronic Materials Section
Department of Chemical Engineering
Delft University of Technology
van der Maasweg 9, 2629 HZ, Delft, The Netherlands
K. Galkowski, Dr. D. K. Maude, Dr. P. Plochocka
Laboratoire National des Champs Magnetiques Intenses
CNRS-UJF-UPS-INSA
143 avenue de Rangueil, 31400 Toulouse, France
K. Galkowski
Faculty of Physics
Institute of Experimental Physics
University of Warsaw - Pasteura 5
02-093 Warsaw, Poland
Prof. R. J. Nicholas
University of Oxford
Clarendon Laboratory
Parks Road, Oxford OX1 3PU, UK
Dr. S. D. Stranks
Cavendish Laboratory
JJ Thomson Avenue, Cambridge CB3 0HE, UK

DOI: 10.1002/adma.201604019

ADVANCED MATERIALS
www.advmat.de

www.MaterialsViews.com

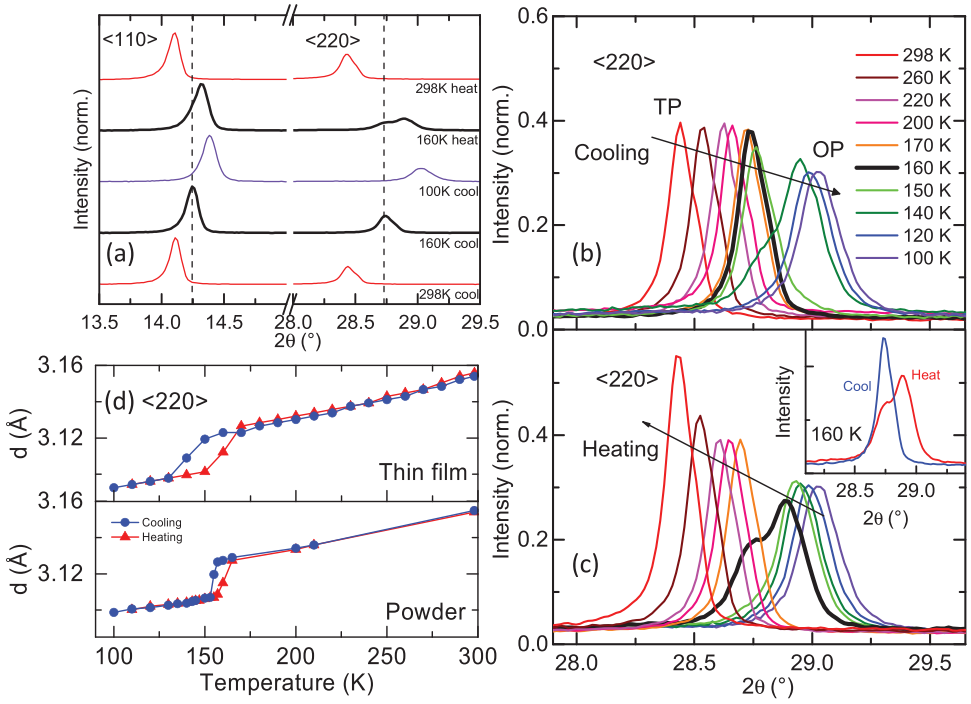

Figure 1. Temperature-dependent X-ray diffractograms (XRD) of a $MAPbI_3$ thin film on silicon. a) Snapshots of the regions of interest of the XRD diffractograms when cooling from room temperature to 100 K and heating back to room temperature (bottom to top). Cooling and heating rates were fixed at 6 K min^{-1} and the sample fixed at each temperature for 30 min to stabilize and to take the measurement (effective average rate of ≈0.3 K min^{-1}). Spectra have been scaled to normalize the strongest reflection <110> to 1. The dashed lines are guides to the eye. b,c) Zoom in on the <220> reflection at different temperatures when cooling from 298 to 100 K (b) and heating the film from 100 K back to 298 K (c) . The inset of (c) compares the spectra at 160 K during the cooling and heating cycles. d) Lattice spacing calculated from the 2θ values of the <220> reflections extracted from the XRD spectra for the thin film (upper panel and Figure S1, Supporting Information) and powder (upper panel and Figure S4, Supporting Information), with weighted averages used for mixed peaks.

configurations upon cooling and heating. We use temperature-dependent micro- and macro-PL measurements to show that the hysteresis in the XRD structural measurements is related to a hysteresis of local inclusions of each phase that are influenced by the local environment, and that the hysteresis is also observed in a variety of other optoelectronic properties. Finally, we observe a change in the texture of the films after a cooling/heating cycle, a phenomenon which is absent in measurements on randomly oriented powder samples, and the texture change correlates with a fusing of grains and a substantial increase in the emission from the sample. Our results highlight an intimate relationship between the structure, crystal orientation, and photophysical properties of perovskites and provide insights into the targeted growth of high-quality perovskite films for devices.

Thin films (≈250 nm thickness) of the $MAPbI_3$ perovskite were deposited on glass, quartz or silicon substrates by spin-coating a lead acetate-based precursor solution followed by annealing of the films (see the Experimental Section).[31] The orthorhombic-to-tetragonal and vice versa phase transitions were monitored via the XRD method and the predominant reflections (<110> and <220>) of the films on silicon at different temperatures are shown in **Figure 1**a (see Figure S1 in the Supporting Information for full diffractograms). The diffractograms reveal the structural evolution of the films upon a cooling/heating cycle through the TP–OP phase transition. Here, the films are controllably cooled from room temperature (298 K) to 100 K and then heated back to 298 K. Importantly, we note that the spectral shifts associated with the thermal expansions and contractions of the Si substrates and XRD Al stage are corrected by adjusting the position of the Si K_β reflection to 61.7° for all measured XRD spectra. In addition, the XRD spectra are normalized to the strongest reflection (<110> in this case). The diffractograms indicate clear shifts in the peak positions to higher 2θ angles upon cooling followed by a gradual shift toward lower 2θ angles during the heating cycle. The data can be fitted with the tetragonal I4/mcm space group above 170 K and the orthorhombic Pnma space group below 130 K.[12] In these temperature regions with a single phase, we calculate the thermal volume expansion coefficient to be 3.4×10^{-4} K^{-1}, in agreement with recent reports.[32] The shift in peak positions as well as broadening of the full-width half-maximum upon cooling is indicative of an increase in the film residual stresses upon temperature cycling. Notably, there is a difference in the peak position and shape at 160 K (black) between the spectra acquired upon cooling and heating the sample; this is highlighted with the dashed vertical lines in Figure 1a.

In Figure 1b,c, we zoom in on the <220> reflection when cooling and heating the sample, respectively. Upon cooling (Figure 1b) we see the onset of the TP–OP transition at 150 K (green). However, a mixed phase of both TP and OP is evident at 140 K followed by a predominantly OP below 130 K.

COMMUNICATION

Upon heating (Figure 1c), the peak character remains OP-dominant until 160 K, when it becomes a mixed phase of both and then a predominantly TP above 170 K. In addition, we find that the ratio of <220>/<110> increases upon heating the sample back up to room temperature; this will be discussed in more detail later. These XRD results suggest that both TP and OP coexist at temperatures around the phase transition. Furthermore, the relative fraction of each phase in the temperature range of 140–160 K is not the same when comparing cooling and heating cycles, as evident from the diffractograms at 160 K in Figure 1b,c.

The hysteresis in the structural properties of the thin films upon cooling and heating is visualized in Figure 1d by comparing the lattice spacing parameter d at each temperature for the cooling and heating cycles, computed from the peak positions (2θ) of the <220> reflections at each temperature (see Figure S1 and S2 in the Supporting Information for the <110> reflections, peak positions, and the integrated peak areas). The results show that the TP–OP phase transition, centered at ≈150 K, is a ≈40 K wide transition extending from 170 to 130 K, temperatures in which the film has completed the phase transition on both cooling and heating. We note that the degree of hysteresis depends on the rate of cooling/heating (Figure S3, Supporting Information); for subsequent measurements the cooling and heating rates were kept fixed and symmetric in both directions.

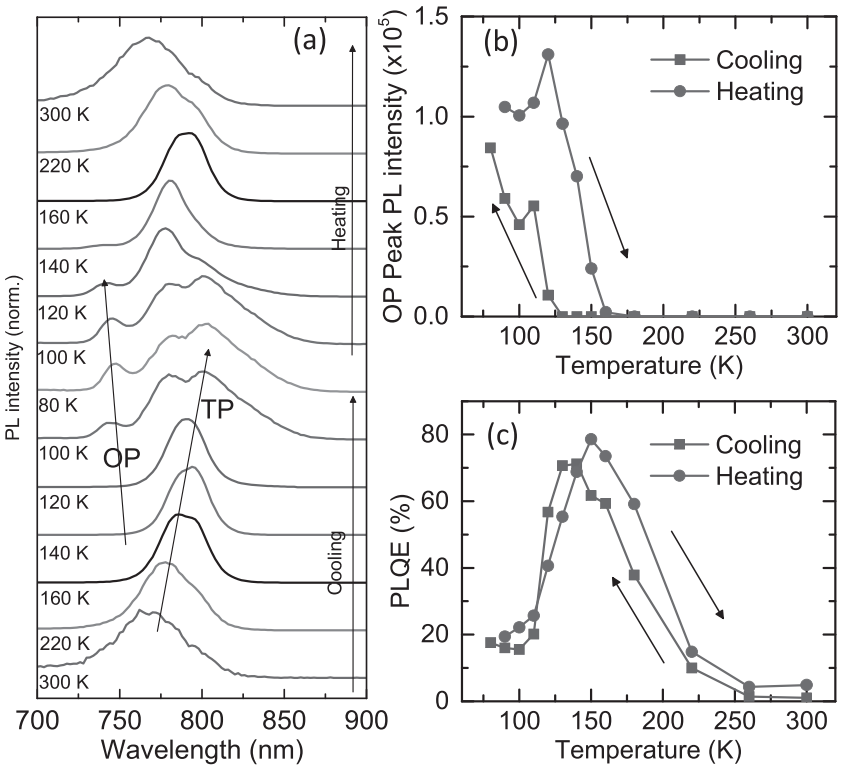

Figure 2. Photoluminescence measurements of thin films. a) Temperature-dependent PL spectra of a MAPbI3 thin film on a quartz substrate when cooling from room temperature to 80 K and back to room temperature (bottom to top). The spectra have been normalized to their peak value. The samples were photoexcited with a 405 nm pulsed laser with a fluence of 2 μJ cm^{-2} pulse^{-1} and a repetition rate of 1 MHz. b) The integrated intensity of the high energy orthorhombic phase (OP ≈ 740 nm) emission peak. c) PL quantum efficiency (PLQE) as a function of temperature when cooling (squares) and heating (circles).

The polycrystalline films have a strong preferential orientation, since the <110> planes are the primary observed reflections (Figure 1a and Figure S1, Supporting Information). To elucidate the effect of the substrate and the preferred grain orientation, we performed the same XRD experiments on powder samples. Here, the powder was obtained by spin-coating thin films on large glass substrates in the same way as for the thin-film samples, but then scraping off the films and grinding to a powder form (see the Experimental Section). The lattice spacing corresponding to the <220> reflections is plotted in Figure 1d (see Figure S4 in the Supporting Information for XRD diffractograms and description). The behavior of the powder with temperature is noticeably different compared to the thin-film sample, with sharper transitions and reduced hysteresis (≈12 K versus ≈40 K for the film), suggesting that the substrate and substrate-induced texture in the film play a significant role in the hysteretic phase phenomena.

In order to investigate how the phase hysteresis is manifested in optoelectronic properties, we performed temperature-dependent macro-PL measurements on $MAPbI_3$ thin films on quartz substrates, which we show in **Figure 2**a (see Figure S5 in the Supporting Information for unnormalized spectra). The TP is characterized by a single emission peak at an energy just below the bandgap.[18] At around and below the TP transition, a second, higher energy peak is observed corresponding to the OP.[18] Upon cooling from room temperature, we observe a redshift and splitting of the TP emission peak and the emergence of the OP peak (≈740 nm) at ≈120 K which increases in intensity relative to the TP peak. These general observations have been reported elsewhere, though we note that there is not yet consensus on the origin of all features of the low-temperature photophysical structure of $MAPbI_3$.[18,33] We observe significant emission from the TP peak even at 80 K, even though the XRD and absorption (Figure S6, Supporting Information) measurements suggest only a small fraction of the material remains in the TP. As we heat the sample back through the phase transition, we observe hysteresis in the spectra, with the spectral shapes and relative intensities clearly different than on the cooling cycle.

In Figure 2b, we plot the integrated intensity of the OP emission peak with temperature. We find that the feature only becomes resolvable at ≈120 K upon cooling but, upon heating, it remains visible until ≈150 K. In Figure 2c, we show the PL quantum efficiency (PLQE), integrated over all emission peaks, at each temperature through the cooling and heating cycle. We find that the PLQE values also exhibit hysteresis, with the maximum value reached at ≈130 K on the cooling cycle and ≈150 K on the heating cycle. We note that recombination in the

ADVANCED MATERIALS
www.advmat.de

www.MaterialsViews.com

films becomes almost entirely radiative at these peak values, consistent with both our previous observations[6] and also with reports of a maximum in device photovoltage at this temperature.[13,15] However, at lower temperatures the PLQE decreases again, suggesting that there are substantial numbers of nonradiative recombination sites below the TP–OP transition. Interestingly, this decrease in PLQE below the phase transition is in contrast to that reported for single crystals;[33] further work will be required to understand these differences. Moreover, we find that this phase hysteresis is not only manifested in the PL properties but also in a variety of other optoelectronic properties including absorption (Figure S7, Supporting Information) and photoconductance[17] (Figure S8, Supporting Information), suggesting an intimate relationship between structure and optoelectronic properties. We find that the hysteresis effects are also present in $MAPbI_3$ films prepared using other fabrication routes (Figure S9, Supporting Information), suggesting it is a general phenomenon in polycrystalline $MAPbI_3$ films. We also observe exaggerated hysteresis in a mesoporous perovskite film (Figure S8, Supporting Information), which is composed of much smaller crystallites than the pristine planar films.[34] This indicates that smaller grains in general have more exaggerated hysteresis effects than larger grains and this is likely due to the increased fraction of surfaces (grain boundaries) which are the sites of strain between neighboring grains.

In order to understand the PL properties and structural changes on the microscale, we performed micro-PL measurements. We plot the micro-PL maps in **Figure 3**, where the blue color indicates the integrated intensity of the OP peak, which we superimpose on the integrated intensity of the TP peak shown in red (see Figure S10 in the Supporting Information for additional temperatures). Upon cooling to 145 K (Figure 3a), we find that the emission arises only from the TP. As we further cool the sample to 125 K (Figure 3d), we observe the emergence of domains showing additional emission from the OP (blue), with the OP intensity anticorrelating with TP emission intensity.[35] As we further cool the samples, we still see large inclusions of the TP even at 80 K (Figure S10, Supporting Information), consistent with the macro-PL measurements. Visualizing these inclusions gives us a direct explanation for the strong TP emission relative to the OP emission at these temperatures even though XRD (Figure 1) and absorption (Figure S7, Supporting Information) measurements indicate that only a very small fraction of the TP should exist at this temperature. Here, energy transfer from the larger bandgap OP domains to even small inclusions of the lower bandgap TP which subsequently emit will lead to a strong quenching of the OP emission (Figure S11, Supporting Information).[18,35,36] The reduced PLQE below 140 K could in part be related to an inefficient energy transfer process, where at least a fraction of the TP inclusions effectively act as nonradiative "traps" in the OP for one or both carriers. These observations are consistent with our recent work in which we found that recombination in the OP is much faster than in the TP.[17]

Upon heating the sample back to 125 K (Figure 3e), we now observe a larger fraction of emission from the OP, which is illustrated by comparing the spatially averaged spectra upon cooling and heating in Figure 3f. When the sample is heated back to 145 K (Figure 3b), we still see large OP inclusions remaining which only disappear again upon further heating

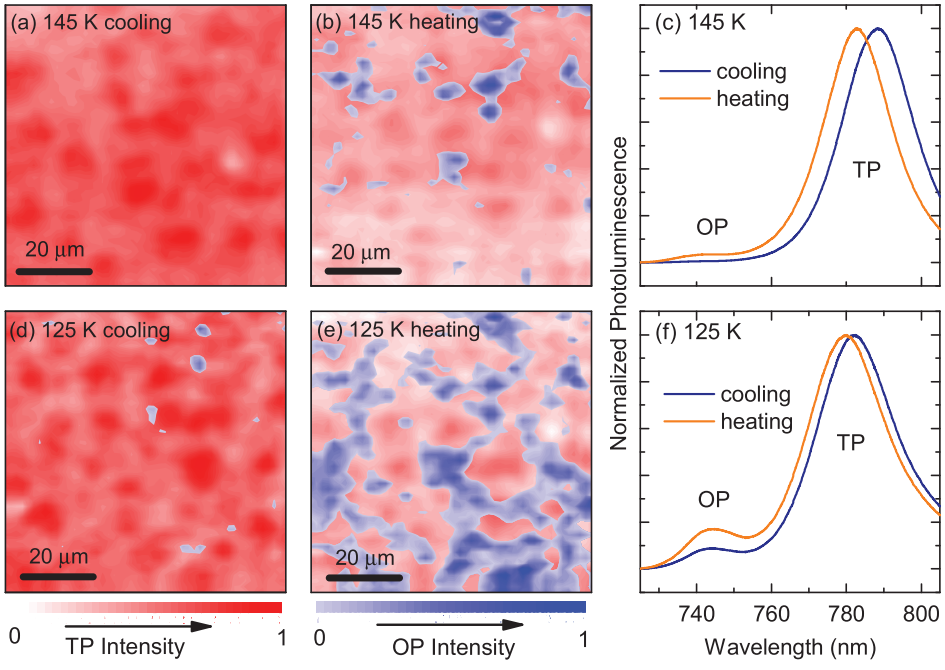

Figure 3. MicroPL maps showing phase hysteresis on the microscale. Spatial microPL maps showing integrated PL intensity from the orthorhombic (OP, blue) and the tetragonal phase (TP, red) peaks. The intensity increases from white to dark blue or red. The scanning step was 2 µm and an illumination intensity of 12 W cm^{-2} was used. Measurements were taking by cooling from room temperature to 145 K (a), 125 K (d), and 80 K then warming back to 125 K (e) and 145 K (b). The spatially averaged spectra are shown at 145 K (c) and 125 K (f).

(Figure S10, Supporting Information). This is substantially different than the spectra upon cooling, which can be seen by comparing the spectra in Figure 3c. These data give us a microscale picture of the phase hysteresis: local regions retain the high temperature phase well below the nominal TP–OP phase transition and other regions retain the OP after warming back to above this temperature. Moreover, the grains which are first to convert to the OP upon cooling act as "seeds" for the further spread of the OP and it is also these seeds that are more likely to stay in the OP at higher temperatures (Figure S10, Supporting Information). We also observe that the presence and intensity of the OP emission is enhanced around a mechanically cracked region of a film relative to the pristine material; the OP peak already appears at higher temperature when cooling than other regions and the OP peak is still considerably strong even after the sample is heated back up to 150 K, whereas the homogeneous material has already predominantly transformed back to the TP at this temperature (Figure S12, Supporting Information). In addition, we note that the absolute emission intensities are enhanced around the crack borders compared to the homogeneous material (Figure S13, Supporting Information).[37] These findings give further evidence that the local environment has a significant influence on the PL properties.

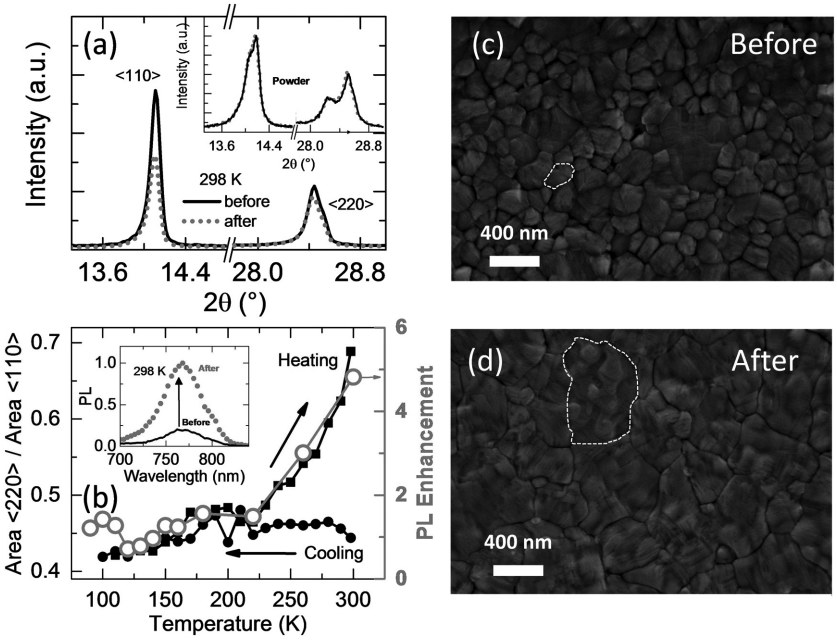

Figure 4. Relationship between grain orientations and emission. a) Zoom in on the <110> and <220> reflections at room temperature before and after the temperature cycle for thin films and powder (inset). b) Ratio of the integrated peak areas of the <220> and <110> reflections from the thin $MAPbI_3$ film diffractograms of Figure 1. The gray open symbols show the PL enhancement of the film for the heating cycle compared to the same temperature on cooling. Inset: PL spectra before and after the temperature cycling, from the thin-film sample at room temperature. c,d) Top-view SEM images of the $MAPbI_3$ films before (c) and after (d) the temperature cycling, with typical grain domains in each highlighted with dashed lines.

Finally, we elucidate the effect of the temperature cycling and how it relates to the structural, morphological, and optoelectronic properties of the thin films. In **Figure 4**a, we plot the X-Ray diffractograms of the thin films measured at room temperature before and after the temperature cycling. We find an overall decrease in the intensities of the reflections after the cycling, with the decrease more prominent for the <110> reflection than the <220> reflection. To further investigate this, we plot the ratios of the integrated peak areas for the <220> and <110> reflections as a function of temperature in Figure 4b, which were extracted from the $MAPbI_3$ thin film diffractograms in Figure 1. We do not see substantial hysteresis in the ratio through the phase transition but we do see a clear increase of the ratio (<220> relative to <110>) for the heating cycle to room temperature relative to the values upon cooling, suggesting the development of the <220> texture as a result of temperature cycling through the phase transition. The texture development is not observed when cycling to a low temperature but still above the phase transition temperature (Figure S14, Supporting Information). Importantly, we do not see this reorientation signature for the powder sample, where the spectra before and after the heating/cooling cycle overlay entirely (Figure 4a, inset). This suggests that the substrate may play a critical role in the realignment of the crystallographic domains and hinder or assist any changes thereof.

We show scanning electron microscopy (SEM) images of the film surfaces before and after the temperature cycling in Figure 4c,d. We find that the grain domains have mostly become fused together after the temperature cycling, with the grain size increasing from a mean of 93 ± 101 nm to a mean fused domain size of 584 ± 275 nm (see Figure S15 in the Supporting Information for grain size distributions). This is a remarkable observation and one we might only expect on annealing the sample at high temperature rather than when cooling the sample below room temperature.

Interestingly, the texture development and grain fusing in the thin film correlate with a large increase in the PL intensity as we heat it back to room temperature (Figure 4b, black open symbols). When comparing the emission at room temperature before and after the temperature cycling (Figure 4b inset), we find that the PL can be enhanced by a factor of 5, corresponding to the increase in PLQE from 1% to 5% seen in Figure 2d.

Our results suggest that the cooling/heating temperature cycle has substantially reduced the fraction of nonradiative recombination channels. It is highly likely that these changes are related to the altered structure and increase in grain size. This is consistent with results reported by D'Innocenzo et al., where films with larger grain sizes were observed to have longer PL lifetimes and enhanced emission intensities.[38] Others have reported that larger grain sizes result in superior solar cell performances,[39] which is consistent with grain boundaries being detrimental to optoelectronic behavior.[23]

The precise mechanism of the grain "fusing" is unclear but we observe that the effects are most prominent when cycling below the phase transition temperature, suggesting that the

structural rearrangements associated with the TP–OP phase transition are critical. The fusing could also be related to the local chemistry of the grain boundaries and how this is affected in the OP, which may in turn be related to the specific origin of the nonradiative decay sites (see the Supporting Information for further discussion). The role that even trace amounts of PbI_2 could play on the fusing, texture development, and hysteresis properties is also presently unclear. Future work to understand this fusing mechanism could elucidate a promising pathway toward polycrystalline perovskite films with substantially reduced nonradiative decay and superior performance.

The structural and hysteretic results presented herein have direct implications for perovskite optoelectronic devices such as solar cells and light-emitting diodies (LEDs). Leblebici et al. recently reported that, within individual grains, there is spatial heterogeneity in the local short-circuit photocurrent and open-circuit photovoltage in polycrystalline $MAPbI_3$ perovskite solar cells.[28] They attributed these variations to different crystal facets and they speculate that the optoelectronic heterogeneity is related to a facet-dependent density of trap states. Our results are consistent with this assertion, where we find a strong link between the optoelectronic behavior (emission) and the preferred orientation of the grain structure. Although the optimal preferred orientation remains unclear, our work reveals that an optimization route focusing on the controlled growth of specifically oriented crystals, potentially on oriented substrates or contacts, would lead to enhanced perovskite material quality and device performance.

In conclusion, we have used bulk XRD measurements to reveal a substantial hysteresis in the phase behavior in $MAPbI_3$ upon cooling and heating. The hysteresis is particularly exaggerated in polycrystalline thin films on substrates and is less significant for a powder sample. Additionally, we find that there is a reorientation signature after the cooling/heating cycle for the polycrystalline film, which leads to enhanced emission properties. This reorientation is absent for the powder sample, suggesting that the substrate may play a critical role in the alignment of and changes to the crystallographic domains. Using microPL mapping, we find that there are emitting inclusions of the TP below the nominal TP–OP transition and, upon heating, we still observe small inclusions of the OP, giving a microscopic picture of the hysteresis effects. Mechanically scratched regions exhibit brighter emission, particularly at low temperature and an earlier (higher) temperature onset of the phase transition compared to the homogeneous regions. Finally, we show that this hysteresis in structure is also manifested in a variety of optoelectronic properties including absorption, PL, and photoconductance, revealing an intimate relationship between structure and performance. Our results indicate that optimizing the grain size and crystal orientation would lead to superior perovskite material and device performance.

Experimental Section

Sample Preparation: Glass/quartz substrates were washed sequentially with soap, deionized figurewater, acetone, and isopropyl alcohol, and finally treated under oxygen plasma for 10 min. Thin films of $CH_3NH_3PbI_3$ were solution-processed by employing a methylammonium iodide (CH_3NH_3 I; MA) and lead acetate $Pb(Ac)_2{\cdot}3H_2O$ precursor mixture. MAI (Dyesol) and $Pb(Ac)_2{\cdot}3H_2O$ (Sigma–Aldrich) were dissolved in anhydrous *N*,*N*-dimethylformamide at a 3:1 molar ratio with final concentration of 37 wt%. The precursor solution was spin-coated at 2000 rpm for 45 s in a nitrogen-filled glovebox and the substrates were then dried at room temperature for 10 min before annealing at 100 °C for 5 min. For the powder samples, the precursor solution was spin-coated onto large glass wafers (≈10 cm diameter) at 1500 rpm followed by the same annealing procedure. The powder (≈30 mg) was obtained by scratching the film off with a knife blade from 5 of the large wafers. All samples were then stored in a nitrogen-filled glovebox until used.

X-Ray Diffraction Measurements: X-ray diffractograms were collected from $MAPbI_3$ thin films on boron-doped Si(100) substrates and $MAPbI_3$ powder samples using a PANalytical X'Pert Pro multi-purpose diffractometer operated at 40 kV and 45 mA (Cu K_α radiation, 1.5418 Å) in Bragg–Brentango geometry. An Oxford Cryosystems PheniX cryostat was employed during nonambient measurement with cooling rate of 6 K min^{-1} (unless otherwise specified). Data was collected with a step size of 0.02° and a scan rate of 1° min^{-1}. Data analysis was carried out using the Panalytical X'pert Highscore Plus program and corrections for stage and substrate thermal expansion during the cooling–heating cycles were made by adjusting the position of Si Kb reflection to the reference value.

Micro-Photoluminescence Measurements: For the microPL measurements the sample was placed in a helium flow cryostat with optical access. Excitation and collection was implemented using a microscope objective with a numerical aperture, NA = 0.55 and magnification 50×. The typical diameter of the spot was of the order of 1 µm. Additionally, the cryostat was mounted on motorized *x*–*y* translation stages to allow high resolution spatial mapping. The microPL spectra were recorded using a spectrometer equipped with a CCD camera. A green solid-state laser, emitting at 532 nm, was used for excitation.

For each thermal cycle, the temperature extremes were 80 and 295 K. The results presented in Figure 3 were obtained through a series of scans performed at 200, 164, 145, 125, and 105 K for both cooling and heating phases of the thermal cycling (155, 145, 140, 130, 120, 110, and 80 K for the mapping series in Figure S10, Supporting Information). The temperature change was set at a rate of 2 K min^{-1}, with the start of each scan delayed by 5 min in order to stabilize the temperature of the sample mount. Typical duration of a single scan was ≈50 min.

Bulk Photoluminescence Measurements: For the temperature-dependent bulk PL measurements the samples were placed in a nitrogen-filled cryostat. At each desired temperature, the samples were fixed for 15 min to stabilize. The PL emission spectra were recorded using an Edinburgh LifeSpec spectrometer. The $MAPbI_3$ films were excited at 405 nm with a picosecond pulsed diode laser (Hamamatsu, M8903-01, $I_0 = 4 \times 10^{12}$ photons cm^{-2}, repetition rate 1 MHz) and emission spectra were recorded in the range 700–900 nm, using a monochromator with 1 nm slits.

The PLQE at room temperature was measured using an integrating sphere in a nitrogen-filled glovebox using a 532-nm excitation laser at an illumination intensity of ≈100 mW cm^{-2} and the PLQE at other temperatures determined scaled relative to this room temperature measurement by accounting for the absorption and PL spectra at each temperature.

Supporting Information

Supporting Information is available from the Wiley Online Library or from the author.

Acknowledgements

This work was supported by the Netherlands Organization for Scientific Research (NWO) under the Echo grant number: 712.014.007. S.D.S. has received funding from the People Programme (Marie Curie Actions) of the European Union's Seventh Framework Programme (FP7/2007-2013) under REA grant agreement number PIOF-GA-2013-622630. This work made use of the shared experimental facilities supported in part by the MRSEC Program of the National Science Foundation under award

number MDR – 1419807. The authors thank Mengfei Wu and Marc Baldo for access to an integrating sphere and Charles Settens for expert assistance with XRD measurements. This work was partially supported by the Region Midi-Pyrenees, the Programme Investissements d'Avenir under the contract MESR, 13053031, project BLAPHENE under IDEX program Emergence, ANR JCJC project milliPICS. The work was also partially supported by Eni S.p.A. via the Eni-MIT Solar Frontiers Center.

Received: July 28, 2016
Revised: September 10, 2016
Published online: October 19, 2016

[1] a) S. D. Stranks, H. J. Snaith, *Nat. Nanotechnol.* **2015**, *10*, 391; b) B. R. Sutherland, E. H. Sargent, *Nat. Photonics* **2016**, *10*, 295; c) M. B. Johnston, *Nat. Photonics* **2015**, *9*, 634.

[2] F. Deschler, M. Price, S. Pathak, L. E. Klintberg, D.-D. Jarausch, R. Higler, S. Hüttner, T. Leijtens, S. D. Stranks, H. J. Snaith, M. Atatüre, R. T. Phillips, R. H. Friend, *J. Phys. Chem. Lett.* **2014**, *5*, 1421.

[3] S. D. Stranks, P. K. Nayak, W. Zhang, T. Stergiopoulos, H. J. Snaith, *Angew. Chem., Int. Ed.* **2015**, *54*, 3240.

[4] a) S. D. Stranks, G. E. Eperon, G. Grancini, C. Menelaou, M. J. Alcocer, T. Leijtens, L. M. Herz, A. Petrozza, H. J. Snaith, *Science* **2013**, *342*, 341; b) G. Xing, N. Mathews, S. Sun, S. S. Lim, Y. M. Lam, M. Gratzel, S. Mhaisalkar, T. C. Sum, *Science* **2013**, *342*, 344.

[5] S. De Wolf, J. Holovsky, S.-J. Moon, P. Löper, B. Niesen, M. Ledinsky, F.-J. Haug, J.-H. Yum, C. Ballif, *J. Phys. Chem. Lett.* **2014**, *5*, 1035.

[6] S. D. Stranks, V. M. Burlakov, T. Leijtens, J. M. Ball, A. Goriely, H. J. Snaith, *Phys. Rev. Appl.* **2014**, *2*, 034007.

[7] a) L. M. Pazos-Outón, M. Szumilo, R. Lamboll, J. M. Richter, M. Crespo-Quesada, M. Abdi-Jalebi, H. J. Beeson, M. Vrućinić, M. Alsari, H. J. Snaith, B. Ehrler, R. H. Friend, F. Deschler, *Science* **2016**, *351*, 1430; b) O. D. Miller, E. Yablonovitch, S. R. Kurtz, *IEEE J. Photovoltaics* **2012**, *2*, 303.

[8] D. A. Egger, A. M. Rappe, L. Kronik, *Acc. Chem. Res.* **2016**, *49*, 573.

[9] a) D. W. deQuilettes, W. Zhang, V. M. Burlakov, D. J. Graham, T. Leijtens, A. Osherov, V. Bulovic, H. J. Snaith, D. S. Ginger, S. D. Stranks, *Nat. Commun.* **2016**, *7*, 11683; b) Y. H. Deng, Z. G. Xiao, J. S. Huang, *Adv. Energy Mater.* **2015**, *5*, 1500721, DOI: 10.1002/aenm.201500721.

[10] a) T. Leijtens, E. T. Hoke, G. Grancini, D. J. Slotcavage, G. E. Eperon, J. M. Ball, M. De Bastiani, A. R. Bowring, N. Martino, K. Wojciechowski, M. D. McGehee, H. J. Snaith, A. Petrozza, *Adv. Energy Mater.* **2015**, *5*, 1500962, DOI: 10.1002/aenm.201500962; b) Z. Xiao, Y. Yuan, Y. Shao, Q. Wang, Q. Dong, C. Bi, P. Sharma, A. Gruverman, J. Huang, *Nat. Mater.* **2015**, *14*, 193; c) C. Li, S. Tscheuschner, F. Paulus, P. E. Hopkinson, J. Kiessling, A. Kohler, Y. Vaynzof, S. Huettner, *Adv. Mater.* **2016**, *28*, 2446.

[11] a) E. T. Hoke, D. J. Slotcavage, E. R. Dohner, A. R. Bowring, H. I. Karunadasa, M. D. McGehee, *Chem. Sci.* **2015**, *6*, 613; b) R. Gottesman, A. Zaban, *Acc. Chem. Res.* **2016**, *49*, 320.

[12] T. Baikie, Y. N. Fang, J. M. Kadro, M. Schreyer, F. X. Wei, S. G. Mhaisalkar, M. Graetzel, T. J. White, *J. Mater. Chem. A* **2013**, *1*, 5628.

[13] H. Zhang, X. F. Qiao, Y. Shen, T. Moehl, S. M. Zakeeruddin, M. Gratzel, M. K. Wang, *J. Mater. Chem. A* **2015**, *3*, 11762.

[14] C. Quarti, E. Mosconi, J. M. Ball, V. D'Innocenzo, C. Tao, S. Pathak, A. Petrozza, H. Snaith, F. De Angelis, *Energy Environ. Sci.* **2015**, *9*, 155.

[15] T. J. Jacobsson, W. Tress, J. P. Correa-Baena, T. Edvinsson, A. Hagfeldt, *J. Phys. Chem. C* **2016**, *120*, 11382.

[16] R. L. Milot, G. E. Eperon, H. J. Snaith, M. B. Johnston, L. M. Herz, *Adv. Funct. Mater.* **2015**, *25*, 6218.

[17] E. M. Hutter, M. C. Gélvez-Rueda, A. Osherov, V. Bulović, F. C. Grozema, S. D. Stranks, T. J. Savenije, *Nat. Mater.* **2016**, DOI: 10.1038/NMAT4765.

[18] C. Wehrenfennig, M. Z. Liu, H. J. Snaith, M. B. Johnston, L. M. Herz, *Appl. Mater.* **2014**, *2*, 081513.

[19] V. D'Innocenzo, G. Grancini, M. J. Alcocer, A. R. Kandada, S. D. Stranks, M. M. Lee, G. Lanzani, H. J. Snaith, A. Petrozza, *Nat. Commun.* **2014**, *5*, 3586.

[20] K. Galkowski, A. Mitioglu, A. Miyata, P. Plochocka, O. Portugall, G. E. Eperon, J. T.-W. Wang, T. Stergiopoulos, S. D. Stranks, H. J. Snaith, R. J. Nicholas, *Energy Environ. Sci.* **2016**, *9*, 962.

[21] D. Li, G. Wang, H.-C. Cheng, C.-Y. Chen, H. Wu, Y. Liu, Y. Huang, X. Duan, *Nat. Commun.* **2016**, *7*, 11330.

[22] Y. Jiang, A. M. Soufiani, A. Gentle, F. Huang, A. Ho-Baillie, M. A. Green, *Appl. Phys. Lett.* **2016**, *108*, 061905.

[23] D. W. deQuilettes, S. M. Vorpahl, S. D. Stranks, H. Nagaoka, G. E. Eperon, M. E. Ziffer, H. J. Snaith, D. S. Ginger, *Science* **2015**, *348*, 683.

[24] C. G. Bischak, E. M. Sanehira, J. T. Precht, J. M. Luther, N. S. Ginsberg, *Nano Lett.* **2015**, *15*, 4799.

[25] S. Draguta, S. Thakur, Y. V. Morozov, Y. Wang, J. S. Manser, P. V. Kamat, M. Kuno, *J. Phys. Chem. Lett.* **2016**, *7*, 715.

[26] M. J. Simpson, B. Doughty, B. Yang, K. Xiao, Y. Z. Ma, *J. Phys. Chem. Lett.* **2015**, *6*, 3041.

[27] Y. Kutes, Y. Zhou, J. L. Bosse, J. Steffes, N. P. Padture, B. D. Huey, *Nano Lett.* **2016**, *16*, 3434.

[28] S. Y. Leblebici, L. Leppert, Y. Li, S. E. Reyes-Lillo, S. Wickenburg, E. Wong, J. Lee, M. Melli, D. Ziegler, D. K. Angell, D. F. Ogletree, P. D. Ashby, F. M. Toma, J. B. Neaton, I. D. Sharp, A. Weber-Bargioni, *Nat. Energy* **2016**, *1*, 16093.

[29] W. Kong, Z. Ye, Z. Qi, B. Zhang, M. Wang, A. Rahimi-Iman, H. Wu, *Phys. Chem. Chem. Phys.* **2015**, *17*, 16405.

[30] F. Panzer, S. Baderschneider, T. P. Gujar, T. Unger, S. Bagnich, M. Jakoby, H. Bässler, S. Hüttner, J. Köhler, R. Moos, M. Thelakkat, R. Hildner, A. Köhler, *Adv. Opt. Mater.* **2016**, *4*, 917.

[31] W. Zhang, M. Saliba, D. T. Moore, S. K. Pathak, M. T. Horantner, T. Stergiopoulos, S. D. Stranks, G. E. Eperon, J. A. Alexander-Webber, A. Abate, A. Sadhanala, S. Yao, Y. Chen, R. H. Friend, L. A. Estroff, U. Wiesner, H. J. Snaith, *Nat. Commun.* **2015**, *6*, 6142.

[32] a) T. J. Jacobsson, L. J. Schwan, M. Ottosson, A. Hagfeldt, T. Edvinsson, *Inorg. Chem.* **2015**, *54*, 10678; b) S. Singh, C. Li, F. Panzer, K. L. Narasimhan, A. Graeser, T. P. Gujar, A. Kohler, M. Thelakkat, S. Huettner, D. Kabra, *J. Phys. Chem. Lett.* **2016**, *7*, 3014.

[33] H. H. Fang, R. Raissa, M. Abdu-Aguye, S. Adjokatse, G. R. Blake, J. Even, M. A. Loi, *Adv. Funct. Mater.* **2015**, *25*, 2378.

[34] T. Leijtens, S. D. Stranks, G. E. Eperon, R. Lindblad, E. M. Johansson, I. J. McPherson, H. Rensmo, J. M. Ball, M. M. Lee, H. J. Snaith, *ACS Nano* **2014**, *8*, 7147.

[35] K. Galkowski, A. Mitioglu, A. Surrente, Z. Yang, D. K. Maude, P. Kossacki, G. E. Eperon, J. T.-W. Wang, H. J. Snaith, P. Plochocka, R. J. Nicholas, arXiv, **2016**, 1606.03234.

[36] a) H. Wang, L. Whittaker-Brooks, G. R. Fleming, *J. Phys. Chem. C* **2015**, *119*, 19590; b) L. Q. Phuong, Y. Yamada, M. Nagai, N. Maruyama, A. Wakamiya, Y. Kanemitsu, *J. Phys. Chem. Lett.* **2016**, *7*, 2316.

[37] Y. Tian, A. Merdasa, E. Unger, M. Abdellah, K. Zheng, S. McKibbin, A. Mikkelsen, T. Pullerits, A. Yartsev, V. Sundstrom, I. G. Scheblykin, *J. Phys. Chem. Lett.* **2015**, *6*, 4171.

[38] V. D'Innocenzo, A. R. Srimath Kandada, M. De Bastiani, M. Gandini, A. Petrozza, *J. Am. Chem. Soc.* **2014**, *136*, 17730.

[39] a) W. Nie, H. Tsai, R. Asadpour, J. C. Blancon, A. J. Neukirch, G. Gupta, J. J. Crochet, M. Chhowalla, S. Tretiak, M. A. Alam, H. L. Wang, A. D. Mohite, *Science* **2015**, *347*, 522; b) X. Ren, Z. Yang, D. Yang, X. Zhang, D. Cui, Y. Liu, Q. Wei, H. Fan, S. Liu, *Nanoscale* **2016**, *8*, 3816.